Upper Frequency Limits for Vortex Guiding and Ratchet Effects

O.V. Dobrovolskiy,[1,2,*] E. Begun,[3] V.M. Bevz,[2] R. Sachser,[3] and M. Huth[3]

[1] *Faculty of Physics, University of Vienna, Vienna 1090, Austria*

[2] *School of Physics, V. Karazin National University, Kharkiv 61077, Ukraine*

[3] *Institute of Physics, Goethe University, Frankfurt am Main 60438, Germany*

(Received 4 October 2019; revised manuscript received 7 December 2019; accepted 17 January 2020; published 7 February 2020)

The guided and rectified motion of magnetic flux quanta are important effects governing the magnetoresistive response of nanostructured superconductors. While at low ac frequencies these effects are rather well understood, their manifestations at higher ac frequencies remain poorly investigated. Here, we explore the upper frequency limits for guided and rectified net motion of superconducting vortices in epitaxial Nb films decorated with ferromagnetic nanostripes. By combining broadband electrical spectroscopy with resistance measurements, we reveal that the rectified voltage vanishes at a *geometrically defined frequency* of about 700 MHz. By contrast, a vortex-guiding-related low-ac-loss response persists up to about 2 GHz. This value corresponds to the *depinning frequency* f_d^s associated with the washboard pinning potential induced by the nanostripes, which exhibits peaks for commensurate vortex-lattice configurations. By applying a sum of dc and microwave ac currents at an angle α with respect to the nanostripes, the angle dependence of $f_d^s(\alpha)$ is found to be correlated with the angle dependence of the depinning current. In all, our findings suggest that superconductors with higher f_d^s should be favorable for efficient vortex manipulation in the gigahertz ac frequency range.

DOI: 10.1103/PhysRevApplied.13.024012

I. INTRODUCTION

Superconducting elements are important building blocks in quantum information processing [1], circuit quantum electrodynamics [2], and photon detectors for astrophysical applications [3,4]. They form the basis for superconducting qubits [5], resonators [6], and various Josephson [7] and Abrikosov fluxonic devices, such as filters [8], rectifiers [9], generators [10], triodes [11], and bolometers [12]. All these devices are known to suffer from losses due to the motion of magnetic flux quanta. These vortices, unless pinned, increase the noise and bit error rate in superconducting quantum interference devices [13], raise dark count rates in photon detectors [14], and reduce quality factors [15] and power-handling capabilities [16]. Controlling the fluxon dynamics is therefore crucial for the performance of superconducting devices [17,18].

In this regard, the guided and rectified motion of vortices are important effects that allow one to affect the magnetoresistive response of superconductors with nanoengineered vortex-pinning sites [9,17,17–34]. While vortex guiding implies noncollinearity of the velocity of the vortices with the driving force exerted on them by the transport current [19–23], rectified net motion of magnetic flux quanta occurs in systems lacking reflection symmetry—so-called vortex ratchets [9,17,27–33]. At present, these effects in the dc- and low-frequency ac-driven regimes are rather well understood; see, e.g., [35–37] for reviews. At the same time, the manifestation of vortex guiding and ratchet effects at high ac frequencies remains poorly investigated so far. Accordingly, two particular issues are especially relevant for fluxonic applications: (i) up to what ac frequency can Abrikosov vortices be manipulated, and (ii) what types of nanoengineered pinning sites are favorable for boosting the upper frequency limit for their efficient manipulation?

Previously, vortex guiding and ratchet effects have been investigated both experimentally [25,28,30,31,33,34,38] and theoretically [22,24,26,29]. At kilohertz ac frequencies, the vortex dynamics is known to be frequency independent [39], and it begins to depend on the ac frequency in the megahertz range [28,31,32,38]. A weakening of the ratchet effect in nanopatterned superconducting films at several gigahertz was observed experimentally [28,30,33] and addressed theoretically [29]. It was also demonstrated that rectified vortex motion can occur due to asymmetry of the edge barriers of plain [38,40] and nanopatterned [31] films. Finally, periodically arranged pinning sites were demonstrated to modify the vortex dynamics at high vortex velocities [41–43], and a high-frequency ac stimulus was revealed to lead to the inhibition of vortex avalanches [44,45] and to stimulation of superconductivity in the vortex state [46,47].

*oleksandr.dobrovolskiy@univie.ac.at

Recently, the microwave response of systems composed of superconducting and ferromagnetic nanostructures has attracted especial attention [48–55]. Because of the antagonistic spin ordering [56], the interplay of superconductivity and ferromagnetism leads to competing ground states, affecting the spin transport [52] and the dynamics of magnetic-moment excitations [48–55]. Examples of phenomena emerging at microwave frequencies include the generation of superconducting pure spin currents [51], shortening of the quasiparticle charge-imbalance relaxation length across the superconducting transition temperature [50], modifications of the dispersion properties of spin waves [49,54], the formation of magnonic band structures [55], and metamaterial properties [57]. In addition, trajectories of moving flux quanta can be imprinted in a soft magnetic layer [58], and guiding and ratchet effects are also being studied for the whirllike spin textures known as skyrmions [59–61].

Here, by combining broadband electrical spectroscopy with dc voltage measurements, we show that the vortex ratchet effect in Nb films decorated with ferromagnetic Co nanostripes vanishes at a *geometrically defined frequency* f_r of about 700 MHz. This frequency is related to the time needed for a vortex to travel between two neighboring Co nanostripes. By contrast, vortex-guiding-affected microwave excess losses persist up to about 2 GHz, which corresponds to the vortex *depinning frequency* f_d^s [45,62–66] in the washboard pinning-potential landscape induced by the Co nanostripe array. In addition, we observe maxima in the depinning frequency when the vortex lattice is commensurate with the periodic pinning-potential landscape. By comparing the vortex guiding and ratchet effects for different tilt angles of the current with respect to the nanostripes, we deduce the angle dependence of the depinning frequency and find that it is correlated with the angle dependence of the depinning current. Our results suggest that superconductors with stronger pinning (resulting in higher f_d^s) and denser pinning arrays (resulting in higher f_r) should be favorable for efficient vortex manipulation in the gigahertz ac frequency range.

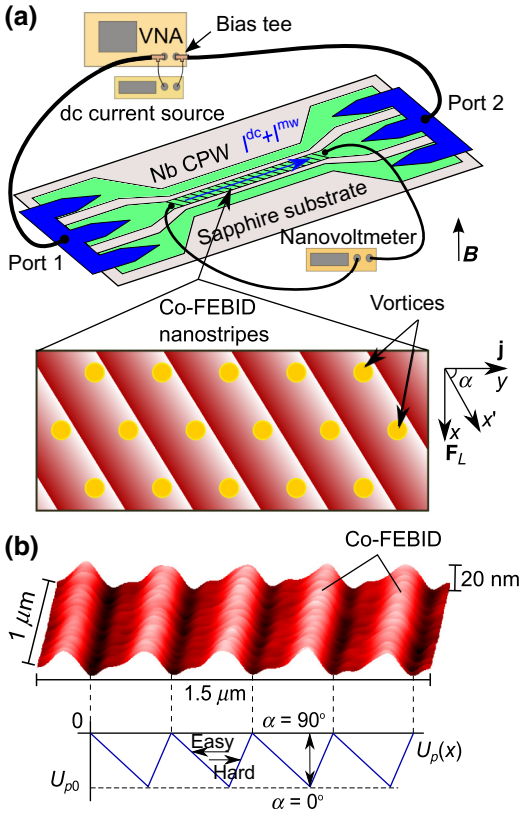

FIG. 1. (a) Experimental geometry: dc and microwave ac currents I^{dc} and I^{mw} are applied to a Nb CPW decorated with an array of Co-FEBID nanostripes. The nanostripes are tilted at an angle α with respect to the CPW axis. The currents exert a Lorentz force $\mathbf{F}_L$ on vortices (denoted by yellow disks), acting along the x axis. The vortex lattice is commensurate with the pinning landscape at 20 mT. For oblique angles $\alpha \neq 0°, 90°$, at sufficiently strong driving forces, the vortices move in the guiding direction x' along the nanostripes. (b) AFM image of the Nb CPW decorated with Co-FEBID nanostripes (top), which induce a pinning potential $U(x)$ of washboard type with a depth U_{p0} and a period 300 nm (bottom). With an increase in α, U_{p0} decreases, and vanishes at 90°. The vortex motion against the nanostripes' steep slopes is in the "hard direction," and that against the gentle slopes is in the "easy direction."

II. EXPERIMENT

The geometry of the experiment is shown in Fig. 1(a). The samples are four nanopatterned Nb coplanar waveguides (CPWs) fabricated from a 56-nm-thick epitaxial (110) Nb film sputtered by dc magnetron sputtering onto an a-cut sapphire substrate. In the sputtering process, the film growth rate is about 1 nm/s, the substrate temperature is $T = 850\,°C$, and the Ar pressure is 5×10^{-3} mbar [67]. The CPWs are fabricated by photolithography in conjunction with Ar etching. The samples are characterized by a superconducting transition temperature $T_c = 8.05$ K, an upper critical field at zero temperature $H_{c2}(0) \simeq 1.4$ T, and a coherence length $\xi(0) \approx 15$ nm. The $H_{c2}(0)$ value is deduced from fitting the dependence $H_{c2}(T)$ to the phenomenological law $H_{c2}(T) = H_{c2}(0)[1 - (T/T_c)^2]$. The standard relation $\xi(0) = \{\Phi_0/[2\pi H_{c2}(0)]\}^{1/2}$ is used to estimate the superconducting coherence length. The central conductor of the CPWs is 100 μm long and 30 μm wide, while the gap between the center and ground conductors is 12 μm, to match the 50 Ω impedance of the feed line. The voltage contacts are wire-bonded on top of the center conductor of each CPW.

The central conductor of each CPW is decorated with parallel Co-based nanostripes spaced by 300 nm, directly written by focused electron-beam-induced deposition (FEBID) [43,68,69]. We refer to the Appendix for

further details of the FEBID process. The Co nanostripe array induces a pinning potential of washboard type in the Nb film via local suppression of the superconducting order parameter via the proximity effect. Inspection by atomic force microscopy (AFM) [see Fig. 1(b)] confirms that the targeted 300-nm periodicity of the array of nanostripes and the desired asymmetry of their cross section necessary to break the pinning-strength symmetry under polarity reversal of the current are achieved. The Co nanostripes have a height of 20 nm and a half-height width b of about 100 nm. To investigate the different regimes of guided and rectified motion of vortices, the nanostripes are tilted at angles $\alpha = 0°$, 30°, 60°, and 90° with respect to the current direction. Specifically, the sum of the dc and ac currents applied along the y axis in a magnetic field $\mathbf{B} \equiv \mathbf{B}_z = \mu_0\mathbf{H}$ exerts a Lorentz force per unit length $\mathbf{F}_L = \Phi_0[\mathbf{j} \times \mathbf{z}]$ on a vortex, acting along the x axis. Here, $\mathbf{j}$ is the electric current density and $\mathbf{z}$ is the unit vector in the z direction.

Combined broadband microwave and dc voltage measurements are done at $0.8T_c = 6.44$ K with the magnetic field $\mathbf{H}$ directed perpendicular to the film surface. The dc voltage V and the absolute value of the forward transmission coefficient S_{21} are measured as a function of the value of the dc bias current $I^{\rm dc}$. To simplify the notation, in the following sections we omit the superscript "dc" in $I^{\rm dc}$. The microwave signal is generated and analyzed by an Agilent E5071C vector network analyzer (VNA). To present the vortex-related microwave loss, in what follows we use the notation of the insertion loss, L_i, deduced from the standard relation $L_i \equiv -S_{21}(f, P, H)/S_{21}(f, P, H_{\rm ref})$ [16,28,30,32,46], where $S_{21}(f, P, H_{\rm ref})$ is the frequency- and microwave-power-dependent reference loss at $H_{\rm ref} > H_{c2}$.

III. RESULTS

Figure 2 displays the vortex-related microwave loss with increasing dc current of positive polarity at $H = 20$ mT and four ac frequencies. At this field value, the vortex lattice is commensurate with the nanostripe array, as illustrated in Fig. 1(a). For other angles, to minimize the energy, the vortex lattice is rotated to adapt it to the "channels" of the periodic pinning potential [70]. The data in Fig. 2(a) are acquired at 64.7 MHz, as an example of the quasistatic regime, at an ac power of −60 dBm (1 nW, dashed lines) and −20 dBm (10 μW, solid lines). Figures 2(b)–(d) illustrate the increase in the insertion loss with increase in frequency up to 1.84 GHz, while Figs. 2(e) and (f) present the frequency dependence of the insertion loss at very small and moderately large values of the dc current.

We first consider the reference dotted curves in Fig. 2(a), acquired in the weak-ac-drive limit (−60 dBm). The curves have a smeared step-function shape for 0° and 90°, while those for 30° and 60° have a double-step shape. The presence of two smeared steps in the curves at −60 dBm

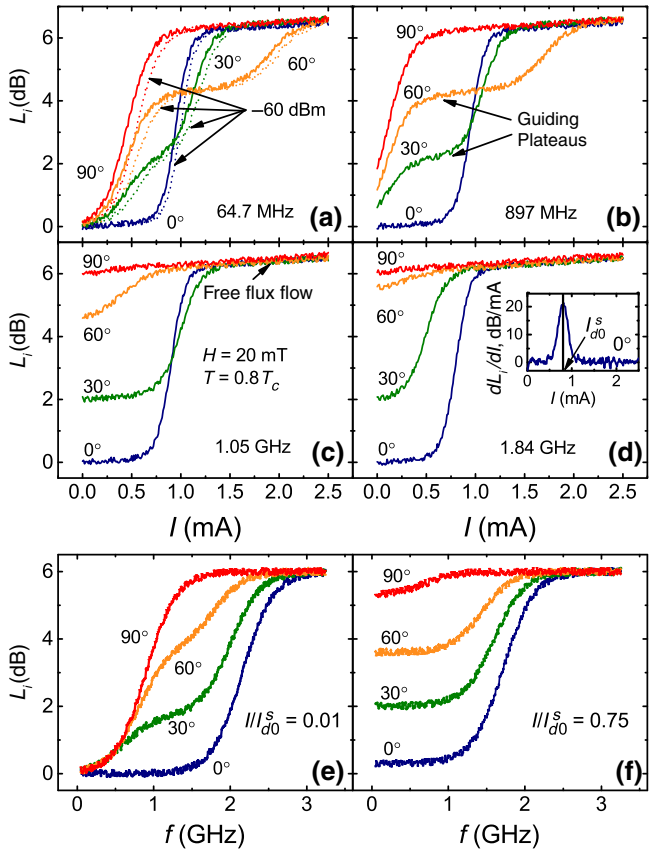

FIG. 2. (a)–(d) Vortex-related insertion loss L_i as a function of the value of the dc current in the presence of an ac current at a power level of −20 dBm (solid lines) for a series of frequencies, as indicated. In (a), the dotted lines correspond to the same measurement of $L_i(I)$ at a power level of −60 dBm. (e),(f) $L_i(f)$ for two values of dc current normalized to the depinning current I^s_{d0}, whose definition is shown in the inset of (d), depicting the current dependence of the derivative of L_i with respect to the current for $\alpha = 0°$. In all panels, $T = 0.8T_c$ and $H = 20$ mT.

in Fig. 2(a) can be understood as a consequence of the coexistence of the intrinsic pinning in the Nb film and the anisotropic pinning induced by the Co nanostripes. Namely, as the dc current increases, the vortices first have to overcome the barriers of the intrinsic pinning, characterized by the depinning current I^i_d. This intrinsic pinning is weak and isotropic, as concluded from $I^i_d(30°) \approx I^i_d(60°) \approx I^i_d(90°) = 0.5$ mA. Here, I^i_d is determined at the maximum of the derivative $d[L_i(I)]/dI$, and we use the same definition of I^s_d as that associated with the washboard pinning potential induced by the Co nanostripes; see the inset of Fig. 2(d). The motion of the vortices at 0° is most efficiently impeded by the nanostripes, and this is why the low-dissipation regime is preserved up to $I^s_{d0} \approx 0.97$ mA. Importantly, $I^s_{d0} \equiv I^s_d(0°) < I^s_d(30°) < I^s_d(60°) \approx 2$ mA, which is a fingerprint of the vortex-guiding effect extensively investigated in the dc-driven regime [19,23,36,71], and which is illustrated further in Fig. 3(a). This effect

consists in the fact that vortices can move along the pinning channels induced by the Co stripes more easily than they can overcome the associated pinning-potential barriers. Given that only the Lorentz-force component acting perpendicularly to the Co stripes drives the vortices across them, one has $I_d^s(\alpha) = I_d^s(0^\circ)/\cos\alpha$ [22]. Accordingly, with $I_d^s(0^\circ) \approx 1$ mA deduced from Fig. 3(a), one obtains $I_d^s(30^\circ) = I_d^s(0^\circ)/\cos 30^\circ \approx 1.16$ mA and $I_d^s(60^\circ) = I_d^s(0^\circ)/\cos 60^\circ \approx 2$ mA, which agrees with the experimental observation. At the same time, at $\alpha = 90^\circ$, the vortices move along the nanostripes and do not experience the washboard pinning potential, which is why $I_d^s(90^\circ)$ cannot be defined. The vortex-related insertion loss at 30° and 60° exhibits plateaus at 0.7 mA $\lesssim I \lesssim$ 0.9 mA and 0.7 mA $\lesssim I \lesssim$ 1.5 mA, respectively. In this regime, $\mathbf{v} \nparallel \mathbf{F}_L$, and the vortices move along the nanostripes [22,36]. Finally, at larger dc currents, the vortices overcome the barriers of the pinning potential induced by the nanostripes, and the regime of free flux flow sets in, with $\mathbf{v} \parallel \mathbf{F}_L$. In the presence of the −20-dBm microwave excitation in Figs. 2(a)–2(d), all crossovers shift towards smaller dc currents.

The evolution of the vortex-related insertion loss with increasing ac frequency is illustrated in Figs. 2(b)–2(d). Specifically, between 64.7 and 897 MHz the addition of the ac current shifts the crossovers related to I_d^i towards smaller currents, whereas the crossovers related to I_d^s remain almost unaffected; see Fig. 2(b). With an increase in the ac frequency to 1.05 GHz, as shown in Fig. 2(c), the curve for $\alpha = 60^\circ$ is shifted to the left and the order of the crossovers at I_d^s for different angles becomes interchanged. With a further increase in f to 1.84 GHz, the most notable change happens to the curve for $\alpha = 30^\circ$, for which now $I_d^s(30^\circ) < I_d^s(0^\circ)$. Finally, when f approaches 2.22 GHz (not shown), L_i reaches about 6 dB at all α and increases very weakly with further increase in the value of the dc current.

For $I/I_{d0}^s = 0.01$, which is an example of the regime of weak dc currents, the frequency dependence of the vortex-related insertion loss is depicted in Fig. 2(e). The curves for $\alpha = 0^\circ$ and 90° qualitatively resemble the well-known results of Gittleman and Rosenblum (GR) [62,65]. In the GR model, the frequency dependence of the microwave power absorbed by vortices at a fixed magnetic field and temperature exhibits a single-step crossover from weak dissipation at low frequencies, where pinning forces dominate, to strong dissipation at high frequencies, where frictional forces prevail. In a manner quite distinct from these GR-like curves, *double-step* crossovers at $\alpha = 30^\circ$ and 60° are clearly seen and allow one to introduce a characteristic depinning frequency for each crossover, at the maximum of its frequency derivative. By contrast, at currents close to the depinning value, an example of which is shown in Fig. 2(f) for $I/I_{d0}^s = 0.75$, single-step crossovers are observed for all α, and the difference between the insertion losses at low and high frequencies becomes smaller with increasing α. This can be understood as a consequence of the effective weakening of the effective periodic pinning potential with increasing α, as the driving force in this case is counterbalanced by the pinning-force component, which is proportional to $\cos\alpha$.

Finally, we present the current-voltage (I-V) curves for all samples in Fig. 3(a), where one can see the crossovers from the pinned and guided regimes to free flux flow in the absence of an ac current. With the superscripts + and − denoting the respective dc-current polarities, we note that $I_d^{s+} > |I_d^{s-}|$ for all $\alpha \neq 90^\circ$ due to the asymmetry of the nanopattern. For $\alpha = 90^\circ$, the depinning current obeys $I_d^{i+} = |I_d^{i-}|$, as expected, as the effective asymmetry of the pinning landscape vanishes in this case. The lower inset of

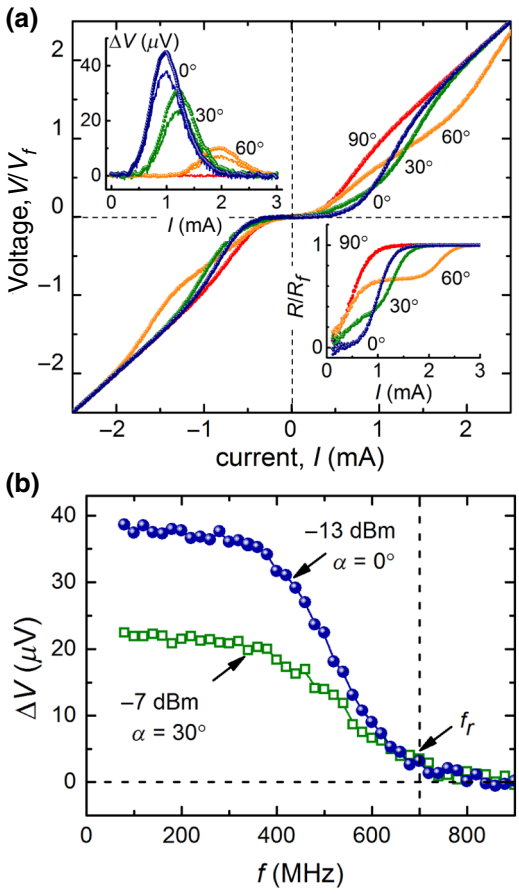

FIG. 3. (a) I-V curves of all samples in the absence of an ac stimulus. Lower inset: current dependence of the normalized resistance. Upper inset: the symbols show the difference voltage $\Delta V = V(I) + V(-I)$ plotted by adding the right-hand and left-hand branches of the respective I-V curves in the main panel, and the solid lines show the rectified dc voltage appearing in the presence of an ac current for $f = 64.7$ MHz. (b) Frequency dependence of the rectified voltage $\Delta V(f)$ for the ac power levels and angles α indicated. The rectified voltage vanishes above $f_r \approx 700$ MHz. In all panels, $T = 0.8T_c$ and $H = 20$ mT.

Fig. 3(a) displays the current dependence of the normalized resistance $R(I)/R_f$, which mimics the shape of the curves in Fig. 2(a). Here, R_f is the flux-flow resistance.

In the absence of a dc current, application of an ac current with $f = 64.7$ MHz results in the appearance of a rectified voltage ΔV of the order of 10 μV for all $\alpha \neq 90°$; see the upper inset in Fig. 3(a). This exception is expected, as at $\alpha = 90°$ the vortices move along the nanostripes, and the asymmetry of the nanostripe slopes does not affect the vortex motion. The rectified voltage $\Delta V(I)$ has a domelike shape as a function of the amplitude of the ac current, and its magnitude decreases with increasing α. For comparison, the reference curves obtained by plotting the difference voltage between the right-hand branch $V(I^+)$ and the left-hand branch $V(I^-)$ of the dc-driven I-V curve in the main panel in Fig. 3(a) are shown by solid lines and resemble the behavior of the $\Delta V(I)$ curves obtained in response to the 64.7-MHz-frequency ac drive. Importantly, the magnitude of the rectified voltage decreases with an increase in the ac frequency and eventually vanishes above $f_r \approx 700$ MHz, as can be concluded from Fig. 3(b).

We note that $\Delta V(I)$ attains its maximum at $I_d^s(0°) \approx 1$ mA and $I_d^s(30°) \approx 1.2$ mA; see the upper inset in Fig. 3(a). Accordingly, the evolution of the maximum $\Delta V(f)$ is shown in Fig. 3(b) for ac currents of 1 and 1.2 mA (corresponding to -13 and -11.5 dBm, respectively) for $\alpha = 0°$ and 30°, respectively. Because of the asymmetry of the I-V curves in Fig. 3(a), we introduce the averaged voltage $\overline{V} = [V(I^+) + |V(I^-)|]/2$, such that 1 mA corresponds to $\overline{V} \approx 0.81$ mV for $\alpha = 0°$ and 1.2 mA corresponds to $\overline{V} \approx 0.99$ mV for $\alpha = 30°$. Employing the standard relation for the vortex velocity $v = \overline{V}/BL$, where $B = 20$ mT and $L = 100$ μm is the distance between the voltage contacts, we deduce $v(0°, 1\text{ mA}) \approx 405$ m/s and $v(30°, 1.2\text{ mA}) \approx 495$ m/s. Following Refs. [30,45], we estimate the displacement of the vortices during one ac period as $2d(0°) = v/f_r$ and $2d(30°) = v\cos 30°/f_r$, yielding $d(0°) \approx 290$ nm and $d(30°) \approx 310$ nm, respectively. This suggests that the rectified voltage vanishes as soon as the amplitude of the vortex oscillations d becomes smaller than the nanopattern period a.

IV. DISCUSSION

We proceed to a discussion of the experimental findings, namely (i) the two-step increase in the insertion loss L_i at $\alpha \neq 0°, 90°$, and (ii) the different upper frequencies for the existence of the rectified voltage (about 700 MHz) and of the low-dissipation microwave response (about 2 GHz at $\alpha = 0°$).

First, it should be recalled that an increase in the vortex-state microwave loss in superconductors is known to occur at the depinning frequency f_d [45,62–66]. This frequency has the physical meaning of a crossover frequency from the low-frequency regime, where the pinning forces dominate and the vortex response is weakly dissipative, to the high-frequency regime, where the frictional forces prevail and the response is strongly dissipative. The experimental data in Fig. 2 point to the presence of *two different* depinning frequencies in our system, f_d^i and f_d^s. The frequency f_d^i can be attributed to the intrinsic pinning in the Nb film, while f_d^s can be attributed to the periodic pinning induced by the Co nanostripes.

To gain further insight into the angle dependences of the depinning frequencies, the insertion loss is measured in the absence of a dc current in the weak-ac-drive regime (-60 dBm) for all samples at magnetic fields varying from -80 to 80 mT. The data for $\alpha = 0°$ are shown in Fig. 4(a). Namely, while the insertion loss increases with an increase in the number of vortices (which is proportional to H), two minima are observed, at 20 and 26.6 mT, on a background with this increase. As mentioned before, 20 mT is a matching field value, at which the vortex lattice is commensurate with the 300 nm periodic nanostripe array. The arrangement of vortices at 20 mT in the pinning nanolandscape is shown in Fig. 1(a) for an assumed triangular vortex lattice with lattice parameter $a_\triangle = (2\Phi_0/B\sqrt{3})^{1/2}$ and the matching condition $a_\triangle = 2a/\sqrt{3}$. In this configuration, all vortices are pinned by the nanostripes, and there are no interstitial vortices. Since all vortices experience the same local pinning forces, the pinning efficiency at the matching field is maximum. We also note that no matching minima in the microwave loss are observed at frequencies above approximately 2 GHz, as will be discussed in what follows.

The dependences of the depinning frequency on the magnetic field in the absence of a dc current for all samples are shown in Fig. 4(b). Namely, $f_d(H)$ exhibits maxima (best seen at 0°) at 6.7, 20, and 26.6 mT and reaches 2.16 GHz at 20 mT. Here, the fields 6.7 and 26.6 mT are further matching fields, satisfying the matching condition $a_\triangle = na$ with order numbers $n = 2$ and $n = 1$, respectively. We refer to Fig. 4(c) for sketches of the vortex-lattice configurations. The data exhibit a systematic decrease with increasing α and a weak decrease with increasing H. With an increase in α, the magnitude of the matching peaks decreases, and the f_d values converge to 1 GHz at large α. The very weak dependence of the depinning frequency on H can be explained by a flattening of the previously observed dependence [64] following the law $f_d = f_d(T, 0, I)[1 - (H/H_{c2})^2]$. This flattening of $f_d(H)$ in our experiment is because the magnetic fields are much smaller than the upper critical field $H_{c2}(0.8T_c) \approx 0.5$ T.

The existence of two depinning frequencies in the decorated Nb films allows us to explain the evolution of the guiding and ratchet effects with increasing ac frequency as follows. With an increase in the tilt angle α of the current with respect to the nanostripes, (i) the *depth* of the effective pinning potential *decreases*, while (ii) its *width increases*. Here, we mean the effective width of the pinning potential

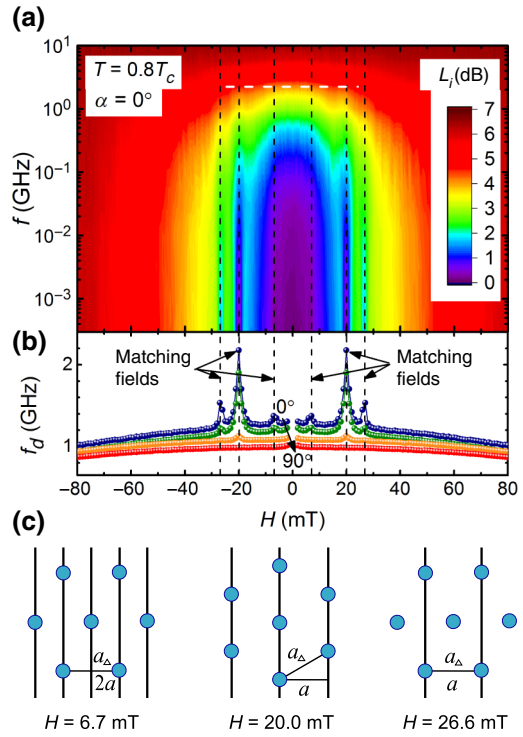

FIG. 4. (a) Insertion loss as a function of the magnetic field and the ac frequency for $\alpha = 0^\circ$. The horizontal dashed line indicates the upper frequency $f \approx 2$ GHz, above which the matching dips vanish. (b) Depinning frequency f_d as a function of the magnetic field at $T = 0.8T_c$ in the absence of a dc current for all angles α. (c) Vortex-lattice configurations at the three matching fields corresponding to the peaks in $f_d(H)$ in (b).

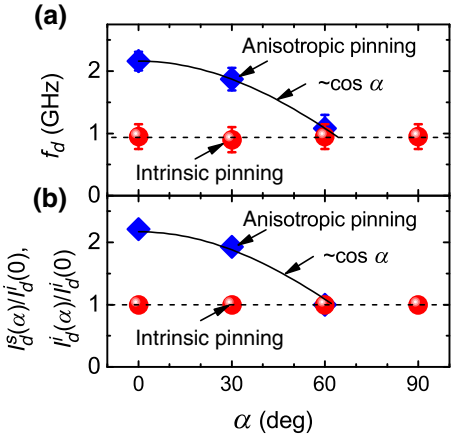

FIG. 5. Angle dependences of the depinning frequencies and normalized depinning currents for intrinsic and anisotropic pinning at $T = 0.8T_c$ and $B = 20$ mT. The solid lines are fits proportional to $\cos\alpha$.

in the direction of the driving force, since it is this effective width which is of primary importance for the excess ac loss associated with oscillation of the vortices at the bottoms of the pinning-potential wells induced by the Co nanostripes. Accordingly, Fig. 5(a) and Fig. 5(b) illustrate a correlation of the depinning frequency with the depinning current for each of the pinning types in the system investigated. Thus, for the background isotropic pinning, both the depinning current and the depinning frequency are independent of α. By contrast, both the depinning current and the depinning frequency for the washboard pinning potential induced by the Co stripes decrease proportionally to $\cos\alpha$ with increasing α, which can be understood as a consequence of a weakening of the normal component of the pinning force impeding the vortex motion.

From previous work, it is known that the depinning frequency depends on the temperature as $f_d \equiv f_d(T,H,I) = f_d(0,H,I)[1-(T/T_c)^4]$ [66] and on the magnetic field as $f_d = f_d(T,0,I)[1-(H/H_{c2})^2]$ [64]. Furthermore, it has been revealed to depend on the dc bias current as $f_d = f_d(T,H,0)[1-(I/I_d)^{3/2}]^{2/3}$ and $f_d = f_d(T,H,0)[1-(I/I_d)^4]^{1/4}$ for the "easy" and "hard" directions, respectively, of the vortex motion [72], for washboard pinning landscapes with an asymmetry which is very close to the one used here. From $f_d(0.8T_c, 0.04H_{c2}) \approx 2.16$ GHz, deduced from Fig. 4, we estimate a zero-temperature value $f_d(0, 0.04H_{c2}) \approx 3.6$ GHz. This estimate correlates reasonably well with our previous experiments on a Nb film with nanogroove arrays milled with a focused ion beam [8].

We emphasize that with increasing ac frequency, the rectified voltage ΔV vanishes at about 700 MHz, while the low-dissipation microwave response persists up to about 2 GHz. To explain the difference between these two frequencies, we compare our experiment with an experiment [30] on $YBa_2Cu_3O_{7-\delta}$ (YBCO) films and outline their distinctive features. Namely, in Ref. [30] the upper frequency limits for vortex guiding and the ratchet effect were investigated on YBCO thin films patterned with antidot arrays. The triangular shape and arrangement of the antidots was designed to break the symmetry of the pinning-potential landscape for vortex motion *along* the antidot rows. In that study, the rectified ratchet voltage persisted up to substantially higher frequencies (about 8 GHz) than the frequency at which the guiding-induced microwave loss vanished (about 2 GHz). Because of the discontinuity of the YBCO film with antidots, it was supposed [30] that flux transport at higher frequencies takes place via phase slips through the isthmuses of the antidots, each acting as a narrow superconducting channel. That suggestion explained the absence of a contribution to the microwave loss above 2 GHz while the rectified voltage persisted up to at least 8 GHz.

In contradistinction to that experiment, the order of the upper frequency limits for the rectified voltage (about 700 MHz) and the crossover to the high-microwave-loss state (about 2 GHz) is reversed in our work. We note that in our experiment the film is continuous, as it is not split

into narrow superconducting channels, and the symmetry of the pinning-potential landscape is broken by nanopatterning in the direction *transverse* to the guiding direction of the Co stripes. Accordingly, the roles of the two length scales responsible for the formation of the rectified voltage and the vortex-related microwave loss are notably different from those in Ref. [30]. Namely, these length scales are the nanostructure period $a = 300$ nm for the rectified voltage, and the full width at half height $b \approx 100$ nm as an estimate for the width of the pinning-potential well determining the crossover from the low-dissipation to the high-dissipation regime. Recalling that the vortex-ratchet effect is a net effect, implying that vortices visit *more than one pinning site* (nanostripe) during each ac cycle, we emphasize that guided vortex motion means that vortices move *along one and the same pinning site* (a nanostripe). Accordingly, with increasing ac frequency, first the frequency is reached at which the vortices do not have enough time to get to the neighboring nanostripes, and this corresponds to the vanishing of the rectified voltage. With a further increase in the frequency, the vortices do not have enough time to reach the regions with strong pinning forces. These regions in our system are the areas of the film under the slopes of the Co stripes that induce the maximum gradients in the pinning potential.

Finally, we outline the general significance of the results obtained.

(i) *Ratchet effect and implications for vortex diodes*. While the system investigated can be used as a rectifier up to 700 MHz, the relation between the upper frequency of the ratchet voltage and the nanostructure period, $f_r \sim v/a$, suggests that pinning arrays with a smaller period should result in higher f_r. Since the current state of technology allows the fabrication of sub-100-nm periodic arrays of pinning sites [73], one can anticipate vortex diodes with cutoff frequencies above 10 GHz based on superconducting films featuring small vortex-core sizes in conjunction with high vortex velocities, such as superconducting cuprates [30]. At the same time, the observed correlation of the depinning frequency with the depinning current related to the anisotropic pinning potential, $f_d \sim I_d^s$, means that the low-loss microwave response should persist up to higher frequencies for superconductors with strong periodic pinning.

(ii) *Guiding effect and implications for microwave filters*. An important feature of the microwave response of guided magnetic flux quanta is a two-step crossover from a low-dissipation state to a highly dissipative state at oblique tilt angles $\alpha \neq 0°, 90°$ of the current with respect to the guiding channels of the washboard pinning potential. In addition to the departure from the widely used GR model [62], implying a single-step crossover for superconductors with one type of pinning, this feature not only allows the development of microwave cutoff filters with tailored frequency rolloffs, but also can be used as a fundamental fingerprint of the presence of pinning of different strengths in the system investigated.

(iii) *Matching peaks in the depinning frequency*. The coexistence of two pinning types in superconductors is reflected in the presence of two characteristic (depinning) frequencies in the microwave response. The observed strong dependence of the depinning frequency on the magnetic field near the matching values (about 250 MHz/mT for the fundamental matching field) may provide a sensitive approach to the determination of commensurate vortex-lattice configurations. This approach is expected to be especially valuable at lower temperatures for superconductors with strong pinning, in which dc resistance measurements at low currents result in voltages below the noise floor of a setup for resolving the particular features of the matching, while at high dc currents the vortex motion causes strong overheating of the superconductor.

(iv) *Implications for hybrid devices based on vortex and spin-wave physics*. There is currently great interest in the microwave properties of hybrid superconductor-ferromagnet systems [49–51,54]. While the Co stripes in our work are used solely as guiding channels for Abrikosov vortices, such an array is expected to behave as a magnonic crystal for spin waves with peculiar Bloch-like band structures in the gigahertz frequency range [74]. While recently it was demonstrated that Co-based FEBID stripes can be used as magnonic conduits [75] and that the interaction of Abrikosov vortices with spin waves leads to the formation of forbidden-frequency gaps in the magnon spectrum [55], one may expect that the spin-wave transmission in such a hybrid system will be modified by guided and rectified vortex motion. The tunability of f_d and f_r should then allow, in principle, the discrimination of characteristic features in the microwave response related to the superconducting and magnetic systems here.

V. CONCLUSION

To summarize, we study by microwave spectroscopy and electrical voltage measurements the guided and rectified motion of magnetic flux quanta in Nb films decorated with Co nanostripes. Excess microwave loss due to vortices guided by the nanostripes is observed at ac frequencies up to about 2 GHz, while the rectified ratchet voltage vanishes already at about 700 MHz. In the system investigated, vortex guiding and the ratchet effect ensue against a background of competition between the intrinsic weak pinning in the Nb film and the strong periodic pinning induced by the Co nanostripe array. Variation of the nanostripe tilt angle with respect to the current direction allows one to distinguish between the two depinning frequencies associated with the two pinning types in the samples. In particular, while $f_d^i \sim 1$ GHz has been revealed to be smaller than $f_d^s \sim 1$–2 GHz and independent of α,

an angle dependence of $f_d^s(\alpha) = f_d^s(0^\circ)\cos\alpha$ is observed. This dependence correlates well with the angle dependence of the depinning current, $I_d^s(\alpha) = I_d^s(0^\circ)\cos\alpha$, associated with the crossover from guided vortex motion along the nanostripes to the regime of free flux flow. In all, the results obtained suggest that superconductors with stronger pinning (resulting in higher f_d^s) and denser pinning arrays (resulting in higher f_r) should be favorable for efficient vortex manipulation in the gigahertz ac frequency range.

ACKNOWLEDGMENTS

O.D. acknowledges the German Research Foundation (DFG) for support through Grant No. 374052683 (DO1511/3-1). Support through the Frankfurt Center of Electron Microscopy (FCEM) is gratefully acknowledged. This work is supported by the European Cooperation in Science and Technology via COST Action CA16218 (NANOCOHYBRI).

APPENDIX

1. Fabrication of Co nanostripes

The Nb CPWs are decorated with Co-based nanostripes by focused electron-beam-induced deposition. FEBID is done in a high-resolution scanning electron microscope (FEI Nanolab 600), employing the precursor gas $Co_2(CO)_8$. This technique relies upon the dissociation of the metal-organic precursor in the focus of the electron beam into a permanent deposit and volatile components, in accordance with the predefined pattern. FEBID of Co is done with beam parameters of 3 kV and 90 pA and 4200 beam passes. The pitch is 10 nm, the dwell time is 1 μs, and the process pressure is 1.1×10^{-5} mbar. Before the deposition, the chamber is evacuated to 6×10^{-6} mbar. The elemental composition of the Co nanostripes is 75 at. % Co, 13 at. % O, and 12 at. % C, as a residue from the precursor, as inferred from energy-dispersive x-ray spectroscopy on thicker replicas of the fabricated structures. Further details of the structural and magnetic properties of the Co structures fabricated by FEBID can be found elsewhere [76]. To break the symmetry in the vortex dynamics under current reversal, the slopes of the nanostripes are designed to be asymmetric. In the patterning process, this is achieved by defining each nanostripe as a five-step "staircase" with a stepwise increasing number of FEBID passes assigned to its "steps." Because of blurring effects, smooth slopes of the nanostripes result instead of the "stairs," as inferred by atomic force microscopy [Fig. 1(b)].

2. Cryogenic spectroscopy measurements

The nanopatterned Nb CPWs have a superconducting transition temperature $T_c = 8.05$ K, as defined by the 90% resistance criterion, and a room-temperature-to-10-K resistance ratio of 4.4. The difference in T_c of different CPWs does not exceed 0.1 K. The upper critical field of all samples at zero temperature, $H_{c2}(0)$, is about 1.4 T, as deduced from fitting the dependence $H_{c2}(T)$ to the phenomenological law $H_{c2}(T) = H_{c2}(0)[1 - (T/T_c)^2]$. This yields a Ginzburg-Landau coherence length $\xi(0) = \Phi_0^{1/2}[2\pi H_{c2}]^{-1/2} \approx 15$ nm, where $\Phi_0 = 2.07 \times 10^{-15}$ T m^2 is the magnetic flux quantum. Combined broadband microwave and dc voltage measurements are done in a ^{4}He cryostat at a temperature of $0.8T_c = 6.44$ K with a magnetic field H directed perpendicular to the film surface. The samples are field cooled before each measurement. Although due to the complex cross-sectional profile of the Co stripes their magnetic state may differ from a single-domain state (with the magnetization directed along the stripe axis), we observe no effect on the pinning potential after the application of out-of-plane and in-plane fields of 2 T.

The samples are mounted in a copper housing in which the pins of micro-SMP connectors are spring-loaded against preformed 300-nm-thick gold contact pads sputtered through a shadow mask onto the film surface after the nanopatterning step. The microwave signal is fed to the sample through coaxial cables from a vector network analyzer (Agilent E5071C). The microwave and dc signals are superimposed and uncoupled by using two bias tees mounted at the VNA ports. The measured quantity is the forward transmission coefficient S_{21}, defined as the ratio (expressed in dB) of the microwave power measured at port 2 to the power transmitted at port 1. While S_{21} is a complex quantity, here we use the notation S_{21} to refer to its absolute value. The depinning frequency f_d can be determined from the complex transmission coefficient at the point where the phase difference between the viscous and pinning forces is $\pi/2$. This definition is equivalent to the definition of f_d as the frequency of the maximum derivative of the insertion loss with respect to f.

[1] M. H. Devoret and R. J. Schoelkopf, Superconducting circuits for quantum information: An outlook, Science **339**, 1169 (2013).

[2] A. Wallraff, D. I. Schuster, A. Blais, L. Frunzio, R.-S. Huang, J. Majer, S. Kumar, S. M. Girvin, and R. J. Schoelkopf, Strong coupling of a single photon to a superconducting qubit using circuit quantum electrodynamics, Nature **431**, 162 (2004).

[3] P. K. Day, H. G. LeDuc, B. A. Mazin, A. Vayonakis, and J. Zmuidzinas, A broadband superconducting detector suitable for use in large arrays, Nature **425**, 817 (2003).

[4] D. Alesini, C. Braggio, G. Carugno, N. Crescini, D. D'Agostino, D. Di Gioacchino, R. Di Vora, P. Falferi, S. Gallo, U. Gambardella, C. Gatti, G. Iannone, G. Lamanna, C. Ligi, A. Lombardi, R. Mezzena, A. Ortolan, R. Pengo,

N. Pompeo, A. Rettaroli, G. Ruoso, E. Silva, C. C. Speake, L. Taffarello, and S. Tocci, Galactic axions search with a superconducting resonant cavity, Phys. Rev. D **99**, 101101(R) (2019).

[5] John Clarke and Frank K. Wilhelm, Superconducting quantum bits, Nature **453**, 1031 (2008).

[6] D. J. Goldie and S. Withington, Non-equilibrium superconductivity in quantum-sensing superconducting resonators, Supercond. Sci. Technol. **26**, 015004 (2012).

[7] A. Barone and S. Pagano, *Josephson Devices* (Springer, Berlin, Heidelberg, 2000).

[8] O. V. Dobrovolskiy and M. Huth, Dual cut-off direct current-tunable microwave low-pass filter on superconducting Nb microstrips with asymmetric nanogrooves, Appl. Phys. Lett. **106**, 142601 (2015).

[9] J. E. Villegas, S. Savel'ev, F. Nori, E. M. Gonzalez, J. V. Anguita, R. Garcia, and J. L. Vicent, A superconducting reversible rectifier that controls the motion of magnetic flux quanta, Science **302**, 1188 (2003).

[10] O. V. Dobrovolskiy, R. Sachser, M. Huth, V. A. Shklovskij, R. V. Vovk, V. M. Bevz, and M. I. Tsindlekht, Radiofrequency generation by coherently moving fluxons, Appl. Phys. Lett. **112**, 152601 (2018).

[11] V. K. Vlasko-Vlasov, F. Colauto, T. Benseman, D. Rosenmann, and W.-K. Kwok, Triode for magnetic flux quanta, Sci. Rep. **6**, 36847 (2016).

[12] S. Lösch, A. Alfonsov, O. V. Dobrovolskiy, R. Keil, V. Engemaier, S. Baunack, G. Li, O. G. Schmidt, and D. Bürger, Microwave radiation detection with an ultra-thin free-standing superconducting niobium nanohelix, ACS Nano **13**, 2948 (2019).

[13] D. Koelle, R. Kleiner, F. Ludwig, E. Dantsker, and John Clarke, High-transition-temperature superconducting quantum interference devices, Rev. Mod. Phys. **71**, 631 (1999).

[14] A. Engel, A. Schilling, K. Il'in, and M. Siegel, Dependence of count rate on magnetic field in superconducting thin-film tan single-photon detectors, Phys. Rev. B **86**, 140506(R) (2012).

[15] C. Song, M. P. DeFeo, K. Yu, and B. L. T. Plourde, Reducing microwave loss in superconducting resonators due to trapped vortices, Appl. Phys. Lett. **95**, 232501 (2009).

[16] N. T. Cherpak, A. A. Lavrinovich, A. I. Gubin, and S. A. Vitusevich, Direct-current-assisted microwave quenching of $YBa_2Cu_3O_{7-x}$ coplanar waveguide to a highly dissipative state, Appl. Phys. Lett. **105**, 022601 (2014).

[17] C.-S. Lee, B. Janko, I. Derenyi, and A.-L. Barabasi, Reducing vortex density in superconductors using the "ratchet effect", Nature **400**, 337 (1999).

[18] O. V. Dobrovolskiy, V. M. Bevz, M. Yu Mikhailov, O. I. Yuzephovich, V. A. Shklovskij, R. V. Vovk, M. I. Tsindlekht, R. Sachser, and M. Huth, Microwave emission from superconducting vortices in Mo/Si superlattices, Nat. Commun. **9**, 4927 (2018).

[19] A. K. Niessen and C. H. Weijsenfeld, Anisotropic pinning and guided motion of vortices in type-II superconductors, J. Appl. Phys. **40**, 384 (1969).

[20] H. Pastoriza, S. Candia, and G. Nieva, Role of Twin Boundaries on the Vortex Dynamics in $YBa_2Cu_3O_7$, Phys. Rev. Lett. **83**, 1026 (1999).

[21] G. D'Anna, V. Berseth, L. Forró, A. Erb, and E. Walker, Scaling of the Hall resistivity in the solid and liquid vortex phases in twinned single-crystal $YBa_2Cu_3O_7 - \delta$, Phys. Rev. B **61**, 4215 (2000).

[22] V. A. Shklovskij and O. V. Dobrovolskiy, Influence of pointlike disorder on the guiding of vortices and the Hall effect in a washboard planar pinning potential, Phys. Rev. B **74**, 104511 (2006).

[23] O. V. Dobrovolskiy, M. Huth, and V. A. Shklovskij, Anisotropic magnetoresistive response in thin Nb films decorated by an array of Co stripes, Supercond. Sci. Technol. **23**, 125014 (2010).

[24] C. J. Olson, C. Reichhardt, B. Jankó, and Franco Nori, Collective Interaction-driven Ratchet for Transporting Flux Quanta, Phys. Rev. Lett. **87**, 177002 (2001).

[25] J. Van de Vondel, C. C. de Souza Silva, B. Y. Zhu, M. Morelle, and V. V. Moshchalkov, Vortex-rectification Effects in Films with Periodic Asymmetric Pinning, Phys. Rev. Lett. **94**, 057003 (2005).

[26] Q. Lu, C. J. Olson Reichhardt, and C. Reichhardt, Reversible vortex ratchet effects and ordering in superconductors with simple asymmetric potential arrays, Phys. Rev. B **75**, 054502 (2007).

[27] M. Velez, J. I. Martin, J. E. Villegas, A. Hoffmann, E. M. Gonzalez, J. L. Vicent, and I. K. Schuller, Superconducting vortex pinning with artificial magnetic nanostructures, J. Magn. Magnet. Mat. **320**, 2547 (2008).

[28] B. B. Jin, B. Y. Zhu, R. Wördenweber, C. C. de Souza Silva, P. H. Wu, and V. V. Moshchalkov, High-frequency vortex ratchet effect in a superconducting film with a nanoengineered array of asymmetric pinning sites, Phys. Rev. B **81**, 174505 (2010).

[29] V. A. Shklovskij, V. V. Sosedkin, and O. V. Dobrovolskiy, Vortex ratchet reversal in an asymmetric washboard pinning potential subject to combined dc and ac stimuli, J. Phys.: Cond. Matt. **26**, 025703 (2014).

[30] R. Wördenweber, E. Hollmann, J. Schubert, R. Kutzner, and G. Panaitov, Regimes of flux transport at microwave frequencies in nanostructured high-T_c films, Phys. Rev. B **85**, 064503 (2012).

[31] D. Cerbu, V. N. Gladilin, J. Cuppens, J. Fritzsche, J. Tempere, J. T. Devreese, V. V. Moshchalkov, A. V. Silhanek, and J. Van de Vondel, Vortex ratchet induced by controlled edge roughness, New J. Phys. **15**, 063022 (2013).

[32] Pedro-de-Jesus Cuadra-Solis, A. Garcia-Santiago, J. M. Hernandez, J. Tejada, J. Vanacken, and V. V. Moshchalkov, Observation of commensurability effects in a patterned thin superconducting Pb film using microwave reflection spectrometry, Phys. Rev. B **89**, 054517 (2014).

[33] O. V. Dobrovolskiy, M. Huth, and V. A. Shklovskij, Alternating current-driven microwave loss modulation in a fluxonic metamaterial, Appl. Phys. Lett. **107**, 162603 (2015).

[34] O. V. Dobrovolskiy, V. A. Shklovskij, M. Hanefeld, M. Zörb, L. Köhs, and M. Huth, Pinning effects on flux flow instability in epitaxial Nb thin films, Supercond. Sci. Technol. **30**, 085002 (2017).

[35] B. L. T. Plourde, Nanostructured superconductors with asymmetric pinning potentials: Vortex ratchets, IEEE Trans. Appl. Supercond. **19**, 3698 (2009).

[36] A. V. Silhanek, J. Van de Vondel, and V. V. Moshchalkov, in *Nanoscience and Engineering in Superconductivity* (Springer-Verlag, Berlin, 2010), Chap. 1, p. 1.

[37] O. V. Dobrovolskiy, Abrikosov fluxonics in washboard nanolandscapes, Phys. C **533**, 80 (2017).

[38] V. V. Pryadun, J. Sierra, F. G. Aliev, D. S. Golubovic, and V. V. Moshchalkov, Plain superconducting films as magnetic field tunable two-dimensional rectifiers, Appl. Phys. Lett. **88**, 062517 (2006).

[39] D. Perez de Lara, L. Dinis, E. M. Gonzalez, J. M. R. Parrondo, J. V. Anguita, and J. L. Vicent, Rocking ratchets in nanostructured superconducting-magnetic hybrids, J. Phys.: Cond. Matter **21**, 254204 (2009).

[40] F. G. Aliev, A. P. Levanyuk, R. Villar, J. F. Sierra, V. V. Pryadun, A. Awad, and V. V. Moshchalkov, Unusual dc electric fields induced by a high frequency alternating current in superconducting nb films under a perpendicular magnetic field, New J. Phys. **11**, 063033 (2009).

[41] A. V. Silhanek, A. Leo, G. Grimaldi, G. R. Berdiyorov, M. V. Milosevic, A. Nigro, S. Pace, N. Verellen, W. Gillijns, V. Metlushko, B. Ili, X. Zhu, and V. V. Moshchalkov, Influence of artificial pinning on vortex lattice instability in superconducting films, New J. Phys. **14**, 053006 (2012).

[42] V. A. Shklovskij, A. P. Nazipova, and O. V. Dobrovolskiy, Pinning effects on self-heating and flux-flow instability in superconducting films near T_c, Phys. Rev. B **95**, 184517 (2017).

[43] O. V. Dobrovolskiy, V. M. Bevz, E. Begun, R. Sachser, R. V. Vovk, and M. Huth, Fast Dynamics of Guided Magnetic Flux Quanta, Phys. Rev. Appl. **11**, 054064 (2019).

[44] A. A. Awad, F. G. Aliev, G. W. Ataklti, A. Silhanek, V. V. Moshchalkov, Y. M. Galperin, and V. Vinokur, Flux avalanches triggered by microwave depinning of magnetic vortices in Pb superconducting films, Phys. Rev. B **84**, 224511 (2011).

[45] A. Lara, F. G. Aliev, V. V. Moshchalkov, and Yu. M. Galperin, Thermally Driven Inhibition of Superconducting Vortex Avalanches, Phys. Rev. Appl. **8**, 034027 (2017).

[46] A. Lara, F. G. Aliev, A. V. Silhanek, and V. V. Moshchalkov, Microwave-stimulated superconductivity due to presence of vortices, Sci. Rep. **5**, 9187 (2015).

[47] O. V. Dobrovolskiy, R. Sachser, V. M. Bevz, A. Lara, F. G. Aliev, V. A. Shklovskij, A. I. Bezuglyj, R. V. Vovk, and M. Huth, Reduction of microwave loss by mobile fluxons in grooved Nb films, Phys. Stat. Sol. - RRL **13**, 1800223 (2019).

[48] C. Bell, S. Milikisyants, M. Huber, and J. Aarts, Spin Dynamics in a Superconductor-ferromagnet Proximity System, Phys. Rev. Lett. **100**, 047002 (2008).

[49] Igor A. Golovchanskiy, Nikolay N. Abramov, Vasily S. Stolyarov, Vitaly V. Bolginov, Valery V. Ryazanov, Alexander A. Golubov, and Alexey V. Ustinov, Ferromagnet/superconductor hybridization for magnonic applications, Adv. Func. Mater. **28**, 1802375 (2018).

[50] Kun-Rok Jeon, Chiara Ciccarelli, Hidekazu Kurebayashi, Jöerg Wunderlich, Lesley F. Cohen, Sachio Komori, Jason W. A. Robinson, and Mark G. Blamire, Spin-pumping-induced Inverse Spin Hall Effect in Nb/ni_80fe_20 Bilayers and its Strong Decay across the Superconducting Transition Temperature, Phys. Rev. Appl. **10**, 014029 (2018).

[51] Kun-Rok Jeon, Chiara Ciccarelli, Andrew J. Ferguson, Hidekazu Kurebayashi, Lesley F. Cohen, Xavier Montiel, Matthias Eschrig, Jason W. A. Robinson, and Mark G. Blamire, Enhanced spin pumping into superconductors provides evidence for superconducting pure spin currents, Nat. Mater. **17**, 499 (2018).

[52] Se Kwon Kim, Roberto Myers, and Yaroslav Tserkovnyak, Nonlocal Spin Transport Mediated by a Vortex Liquid in Superconductors, Phys. Rev. Lett. **121**, 187203 (2018).

[53] K. Rogdakis, A. Sud, M. Amado, C. M. Lee, L. McKenzie-Sell, K. R. Jeon, M. Cubukcu, M. G. Blamire, J. W. A. Robinson, L. F. Cohen, and H. Kurebayashi, Spin transport parameters of nbn thin films characterized by spin pumping experiments, Phys. Rev. Mater. **3**, 014406 (2019).

[54] I. A. Golovchanskiy, N. N. Abramov, M. Pfirrmann, T. Piskor, J. N. Voss, D. S. Baranov, R. A. Hovhannisyan, V. S. Stolyarov, C. Dubs, A. A. Golubov, V. V. Ryazanov, A. V. Ustinov, and M. Weides, Interplay of Magnetization Dynamics with a Microwave Waveguide at Cryogenic Temperatures, Phys. Rev. Appl. **11**, 044076 (2019).

[55] O. V. Dobrovolskiy, R. Sachser, T. Brächer, T. Böttcher, V. V. Kruglyak, R. V. Vovk, V. A. Shklovskij, M. Huth, B. Hillebrands, and A. V. Chumak, Magnon-fluxon interaction in a ferromagnet/superconductor heterostructure, Nat. Phys. **15**, 477 (2019).

[56] J. Linder and J. W. A. Robinson, Superconducting spintronics, Nat. Phys. **11**, 307 (2015).

[57] A. Pimenov, P. Przyslupski, A. Loidl, and B. Dabrowski, Negative Refraction in Ferromagnet-superconductor Superlattices, Phys. Rev. Lett. **95**, 247009 (2005).

[58] G. Shaw, A. S. Blanco, J. Brisbois, L. Burger, L. B. L. G. Pinheiro, R. B. G. Kramer, M. Motta, K. Fleury-Frenette, W. A. Ortiz, B. Vanderheyden, and A. V. Silhanek, Magnetic recording of superconducting states, Metals **9**, 1022 (2019).

[59] W. S. Lew, W. L. Gan, I. Purnama, and F. Ma, *Magnetic Skyrmion Channels: Guided Motion in Potential Wells* (Taylor & Francis Group, Boca Raton, London, New York, 2016), Chap. 13, p. 28.

[60] X. Ma, C. J. Olson Reichhardt, and C. Reichhardt, Reversible vector ratchets for skyrmion systems, Phys. Rev. B **95**, 104401 (2017).

[61] Weijin Chen, Linjie Liu, and Ye Ji Yue Zheng, Skyrmion ratchet effect driven by a biharmonic force, Phys. Rev. B **99**, 064431 (2019).

[62] J. I. Gittleman and B. Rosenblum, Radio-frequency Resistance in the Mixed State for Subcritical Currents, Phys. Rev. Lett. **16**, 734 (1966).

[63] M. Golosovsky, M. Tsindlekht, H. Chayet, and D. Davidov, Vortex depinning frequency in $YBa_2Cu_3O_{7-x}$ superconducting thin films: Anisotropy and temperature dependence, Phys. Rev. B **50**, 470 (1994).

[64] D. Janjušević, M. S. Grbić, M. Požek, A. Dulčić, D. Paar, B. Nebendahl, and T. Wagner, Microwave response of thin niobium films under perpendicular static magnetic fields, Phys. Rev. B **74**, 104501 (2006).

[65] N. Pompeo and E. Silva, Reliable determination of vortex parameters from measurements of the microwave complex resistivity, Phys. Rev. B **78**, 094503 (2008).

[66] A. G. Zaitsev, R. Schneider, G. Linker, F. Ratzel, R. Smithey, and J. Geerk, Effect of flux flow on microwave losses in $YBa_2Cu_3O_{7-x}$ superconducting films, Phys. Rev. B **68**, 104502 (2003).

[67] O. V. Dobrovolskiy and M. Huth, Crossover from dirty to clean superconducting limit in dc magnetron-sputtered thin Nb films, Thin Solid Films **520**, 5985 (2012).

[68] M. Huth, F. Porrati, and O. V. Dobrovolskiy, Focused electron beam induced deposition meets materials science, Microelectr. Eng. **185–186**, 9 (2018).

[69] O. V. Dobrovolskiy, M. Kompaniiets, R. Sachser, F. Porrati, Ch. Gspan, H. Plank, and M. Huth, Tunable magnetism on the lateral mesoscale by post-processing of Co/Pt heterostructures, Beilstein J. Nanotech. **6**, 1082 (2015).

[70] I. Guillamon, R. Cordoba, J. Sese, J. M. De Teresa, M. R. Ibarra, S. Vieira, and H. Suderow, Enhancement of long-range correlations in a 2d vortex lattice by an incommensurate 1d disorder potential, Nat. Phys. **10**, 851 (2014).

[71] O. V. Dobrovolskiy, E. Begun, M. Huth, V. A. Shklovskij, and M. I. Tsindlekht, Vortex lattice matching effects in a washboard pinning potential induced by Co nanostripe arrays, Phys. C **471**, 449 (2011).

[72] O. V. Dobrovolskiy, M. Huth, V. A. Shklovskij, and R. V. Vovk, Mobile fluxons as coherent probes of periodic pinning in superconductors, Sci. Rep. **7**, 13740 (2017).

[73] B. Aichner, B. Müller, M. Karrer, V. R. Misko, F. Limberger, K. L. Mletschnig, M. Dosmailov, J. D. Pedarnig, F. Nori, R. Kleiner, D. Koelle, and W. Lang, Ultradense tailored vortex pinning arrays in superconducting $YBa2Cu3O_{7-\delta}$ thin films created by focused he ion beam irradiation for fluxonics applications, ACS Appl. Nano Mater. **2**, 5108 (2019).

[74] A. V. Chumak, A. A. Serga, and B. Hillebrands, Magnonic crystals for data processing, J. Phys. D: Appl. Phys. **50**, 244001 (2017).

[75] O. V. Dobrovolskiy, R. Sachser, S. A. Bunyaev, D. Navas, V. M. Bevz, M. Zelent, W. Smigaj, J. Rychly, M. Krawczyk, R. V. Vovk, M. Huth, and G. N. Kakazei, Spin-wave phase inverter upon a single nanodefect, ACS Appl. Mater. Interf. **11**, 17654 (2019).

[76] E. Begun, O. V. Dobrovolskiy, M. Kompaniiets, Ch. Gspan, H. Plank, and M. Huth, Post-growth purification of Co nanostructures prepared by focused electron beam induced deposition, Nanotechnology **26**, 075301 (2015).